Computers & Graphics 124 (2024) 104060

Contents lists available at ScienceDirect

Computers & Graphics

journal homepage: www.elsevier.com/locate/cag

Special Section on EG VCBM 2024

Advanced visualization of aortic dissection anatomy and hemodynamics

Aaron Schroeder [a,*], Kai Ostendorf [a], Kathrin Bäumler [b], Domenico Mastrodicasa [c], Veit Sandfort [b], Dominik Fleischmann [b], Bernhard Preim [a], Gabriel Mistelbauer [b]

[a] Department of Simulation and Graphics, Otto-von-Guericke University Magdeburg, Germany
[b] Department of Radiology, Stanford University School of Medicine, CA, United States
[c] University of Washington, WA, United States

ARTICLE INFO

Keywords:
Medical visualization
Hemodynamics
Flow visualization

ABSTRACT

Aortic dissection is a life-threatening cardiovascular disease constituted by the delamination of the aortic wall. Due to the weakened structure of the false lumen, the aorta often dilates over time, which can – after certain diameter thresholds are reached – increase the risk of fatal aortic rupture. The identification of patients with a high risk of late adverse events is an ongoing clinical challenge, further complicated by the complex dissection anatomy and the wide variety among patients. Moreover, patient-specific risk stratification depends not only on morphological, but also on hemodynamic factors, which can be derived from computer simulations or 4D flow magnetic resonance imaging (MRI). However, comprehensible visualizations that depict the complex anatomical and functional information in a single view are yet to be developed. These visualization tools will assist clinical research and decision-making by facilitating a comprehensive understanding of the aortic state. For that purpose, we identified several visualization tasks and requirements in close collaboration with cardiovascular imaging scientists and radiologists. We displayed true and false lumen hemodynamics using pathlines as well as surface hemodynamics on the dissection flap and the inner vessel wall. Pathlines indicate antegrade and retrograde flow, blood flow through fenestrations, and branch vessel supply. Dissection-specific hemodynamic measures, such as interluminal pressure difference and flap compliance, provide further insight of the blood flow throughout the cardiac cycle. Finally, we evaluated our visualization techniques with cardiothoracic and vascular surgeons in two separate virtual sessions.

1. Introduction

Aortic dissection is a rare, life-threatening cardiovascular disease [1], that is characterized by the formation of a secondary blood flow channel, called false lumen, which carves its way through the media layer of the aortic wall. Both flow channels, i.e., true and false lumen, are separated by the dissection flap, a thin and elastic membrane. The weakened outer wall of the false lumen consists of the remaining aortic media and the adventitia. Classification, treatment, and prognosis of aortic dissections strongly depend on morphological features captured by imaging studies [2,3]. However, potential collapse of the true lumen and subsequent malperfusion of the branch vessels are related to the number, size, and location of intimal tears and to the distribution of branch vessels that are draining the false and true lumen, as shown by phantom studies [4,5]. Additionally, increased false lumen pressure possibly promotes false lumen dilation and aortic rupture [6,7]. Limited false lumen outflow was shown to contribute to overall disease progression [8,9].

While the prognostic assessment of patients with aortic dissection primarily still relies on morphological features, the blood flow can be measured and evaluated with 4D flow MRI. Stroke volume, primary entry tears, helical flow, and velocity are found to be related to the rate of aortic expansion [10]. Noninvasive hemodynamic measurements, using 4D flow MRI, provide insight into these functional aspects of a patient's vascular system. However, due to limited availability and high cost, these scans are not routinely obtained. Alternatively, computational fluid dynamics (CFD) simulations provide an increasingly reliable and accessible way to obtain patient-specific hemodynamic data [11,12]. These data could be useful for clinical decision-making, such as timing and selection of drug, endovascular, or surgical treatment, and aid the development of new treatment approaches. Precise and clear visual

* Corresponding author.
E-mail addresses: aaron.schroeder@st.ovgu.de (A. Schroeder), kai.ostendorf@st.ovgu.de (K. Ostendorf), baeumler@stanford.edu (K. Bäumler), mastro@stanford.edu (D. Mastrodicasa), veit.sandfort@stanford.edu (V. Sandfort), d.fleischmann@stanford.edu (D. Fleischmann), bernhard@isg.cs.uni-magdeburg.de (B. Preim), gmistelb@stanford.edu (G. Mistelbauer).

https://doi.org/10.1016/j.cag.2024.104060
Received 3 May 2024; Received in revised form 9 August 2024; Accepted 20 August 2024
Available online 30 August 2024

representation of complex hemodynamic data, however, is pivotal for correct interpretation and treatment.

Efficient and clinically meaningful visualization of the complex anatomical and relevant functional information of aortic dissections poses considerable challenges and has not been adequately addressed. Current visualizations depict only common hemodynamic measures, such as velocity and wall shear stress (WSS). Extending these approaches to the lumina of the dissected aorta is not straightforward, and it is further impacted by luminal communications (fenestrations). Despite preliminary work in this area [13,14], the visualization of multiple aortic wall surfaces with the dissection flap (anatomy) and hemodynamics (function) is still unexplored.

In this paper, we introduce visualization techniques to display presumptive clinically and pathophysiologically relevant morphological and functional information of aortic dissection based on CFD simulation results. The required blood flow simulations were performed according to Bäumler et al. [15]. Besides combining established techniques to create visualizations optimized for the intricate anatomy and hemodynamics of dissections, we also present novel derived measures that yield previously unrecognized insights. Our major technical contributions are:

- Correct mapping of blood flow in true and false lumen, which occasionally intersect, essentially preventing incorrect integration of pathlines through the dissection flap.
- Effective demonstration of dissection flap deformation along with its associated hemodynamic repercussions, such as interluminal pressure difference and flap compliance.
- Display of the impacts of blood flow dynamics, such as flow jets caused by fenestrations, on the weakened false lumen outer wall.

All contributions have been developed through an iterative process in collaboration with our international multidisciplinary team, including cardiovascular imaging experts, experts on computer simulations and experienced cardiovascular radiologists. The clinical innovations of this work enable medical experts to:

- Effectively visualize complex scenarios involving both morphology and hemodynamics, thereby supporting the development of preliminary treatment strategies and precision in device placement.
- Gain a thorough understanding of intricate blood flow dynamics. This understanding mimics the insights gained through catheter angiography, thus providing a viable method for illustrating complex cases.

The results of this work were reviewed and evaluated by cardiothoracic and vascular surgeons specialized in open surgery and endovascular procedures for aortic dissection.

2. Related work

In this section, we discuss CFD simulations and visualizations, combining vessel wall and hemodynamics, and focus-and-context techniques to highlight specific structures while de-emphasizing surrounding tissue.

2.1. Computational fluid dynamic simulations

Patient-specific CFD simulations of aortic dissections are typically based on computed tomography (CT) or MRI scans that are used to create the geometric model and computational mesh. Simulations with rigid wall assumptions showed a correlation of elevated false lumen pressure and WSS with subsequent disease progression [16,17]. Simulations of thoracic endovascular aortic repair also showed increased false lumen pressure with restricted outflow and a reduction in false lumen pressure with restricted inflow [18,19]. Effective visualization of pressure inside the aorta could therefore help to predict disease progression and consolidate the understanding of aortic dissection hemodynamics.

Studies aiming to validate CFD simulations against 4D flow MRI [20] found errors of 20% or more between measured and simulated flow data. Reasons for these errors could be rigid wall assumptions and measurement inaccuracies. To more accurately simulate hemodynamics in aortic dissections, dynamic deformation of the vessel wall and, most importantly, of the dissection flap have to be incorporated into the simulation as they affect pressure differences and other relevant hemodynamic quantities. However, realistic depictions of physiological deformations are challenging, due to the varying thickness and material properties of the vessel wall and external tissue support [15]. Bäumler et al. [15] performed CFD simulations with fluid-structure interaction (FSI) that captured wall and flap motion throughout the cardiac cycle. The simulations were informed by 4D flow MRI data, and results compared to in-vivo measurements.

2.2. Hemodynamics visualization

Oeltze-Jafra et al. [21] performed an extensive survey on visualization of medical flow data. They consider the visual exploration of flow in cerebral aneurysms, the nasal cavity, and the aorta. They also describe medical imaging, segmentation, mesh extraction, and flow data acquisition. In the subsequent paragraphs we describe work specific to rendering multiple vessel wall layers and visualization of hemodynamics.

Gasteiger et al. [22] visualize blood flow in aneurysms by applying a ghosted view approach to the aneurysm surface and line drawings for morphological features. Blood flow is visualized using streamlines and depth perception is improved with shadow casting in conjunction with atmospheric attenuation. Lawonn et al. [23] combine multiple techniques for their visualization of blood flow in aneurysms. They use an improved ghosted view approach with pathlines that are color-coded using a 2D texture lookup table and suggestive contours. Behrendt et al. [24] use a Fresnel-inspired blending mask to simultaneously map surface parameters and pseudo chroma depth to the vessel wall using the color channel. Red and blue colors are reserved for the depth and green for mapping a surface parameter, such as WSS. The pseudo chroma depth is applied using the idea of ghosted views, which employ the Fresnel effect, resulting in a shading that only encodes depth on the edges of the mesh, while displaying the surface parameter on the entire surface.

Behrendt et al. [25] also presented a visual exploration framework for intracranial aneurysms, that employs *glass lighting* to create a transparent vessel wall visualization. It combines the Fresnel effect with traditional Phong lighting, to make internal pathline structures visible, while still displaying vessel wall contours. Pathlines are seeded using evolutionary algorithms based on user-specified regions-of-interest on the vessel wall. This reduces clutter, caused by unwanted pathlines, while also reducing undersampling in important areas. Köhler et al. [26] display pathlines together with a vessel mesh outline and direct volume rendering (DVR) as context. Pathlines can be filtered according to different flow features and criteria while hemodynamic measures are displayed with minimum and maximum intensity projection. However, a simultaneous visualization of both, pathlines and hemodynamic measures with intensity projection, was not investigated. Motivated by this approach, we map hemodynamic measures to the vessel surface instead of using intensity projections. Moreover, our approach allows us to simultaneously display the different aortic wall layers, pathlines, and hemodynamic measures while retaining the spatial anatomical context information.

Visualization of blood flow alone without the corresponding vessel surface is often insufficient. Usually, one aspect can be considered as the focus (e.g., hemodynamics), while the other (the vessel surface) serves as a context to navigate the data and provide an overview.

Table 1
Task-requirement diagram for the design of anatomical and functional displays of dissections. In three use cases (UC), we identified nine tasks (T) modeled with twelve requirements (R). Requirements that necessitated novel approaches are highlight in bold.

visualize the blood flow									T1
	highlight slow/fast flow								T2
		highlight retrograde flow							T3
			visualize drainage pattern						T4
				visualize flap deformation					T5
					visualize interluminal pressure gradients				T6
						visualize dissection flap compliance			T7
							visualize flow through fenestrations		T8
								highlight impingement zones	T9
•	•	•	•				•		**show flow pathlines** R01
•		•							show flow direction R02
•				•	•	•	•		**show dissection flap** R03
•								•	show outer vessel wall R04
	•								highlight slow and fast flow R05
		•							**highlight retrograde flow** R06
			•						**show lumina that supply a vessel branch** R07
				•	•	•			show extent of flap deformation R08
					•				**show interluminal pressure difference** R09
						•			**show flap compliance** R10
							•		avoid obstructing view of flow at fenestrations R11
								•	highlight elevated pressure and WSS R12
T1	T2	T3	T4	T5	T6	T7	T8	T9	
UC1				UC2			UC3		

Straka et al. [27] proposed the *VesselGlyph*, an approach to render vascular structures. They focus on assessing stenotic regions using a tailored visualization of the vessel lumen while providing contextual information using DVR. This concept can also be applied to rendering hemodynamics. Glaßer et al. [28] color-coded WSS on the inner vessel wall and depicted wall thickness using distance ribbons on the outer wall. The vessel's lumen can be assessed by modulating the transparency of the outer vessel wall with the Fresnel effect. Lawonn et al. [29] visualized blood flow (focus) with glyphs together with wall thickness (context) color-coded on the vessel surface. Depending on the current visualization goal, either flow or vessel geometry act as context information.

Specifically for aortic dissection treatment planning, Ostendorf et al. [14] recently assessed different shading styles for the dissection flap and the inner and outer vessel wall. Multiple vessel wall surfaces were also rendered by Mistelbauer et al. [13]. They implicitly modeled arbitrarily shaped cross-sections of aortic dissections and rendered the walls semi-transparently. Apart from rendering the inner and outer aortic wall surfaces, our work includes additional surfaces constituting the dissection flap.

3. Task and requirement analysis

We identified three use cases (UCs) that encapsulate the intricate hemodynamics inherent to aortic dissection. Each UC concentrates on a distinctive aspect of the disease, thus necessitating specialized anatomical and functional visualization techniques. An overview detailing each UC and their associated tasks is presented in Table 1. From these tasks, we derive the requirements for our visualization design. Any requirements where we contributed technically are highlighted in bold. Subsequent paragraphs provide descriptions of the tasks, grouped per UC, including the motivation and background, intended target users, and the expected benefits.

***Use case 1**: Visualization of true and false lumen blood flow in aortic dissection.* Hemodynamic visualizations assist CFD simulation experts to comprehend the interaction between morphology and hemodynamics, and foster hypotheses regarding how blood flow dynamics relate to late adverse events. In cardiothoracic and vascular surgery, visualization is instrumental in devising initial treatment strategies and precise device placement, aiding in mentally mapping the complex interplay between morphology and hemodynamics. Moreover, these visualizations facilitate surgeons in executing treatment approaches, simplifying otherwise intricate structural patterns.

The motivation for such visualizations comes from understanding that acute complications, like branch vessel malperfusion, as well as chronic complications, such as aneurysm formation, are fundamentally tied to blood flow in each channel. Visual representations facilitate understanding these complications (T1). False lumen pressurization, a key driver of false lumen dilation and aortic growth, is potentially related to the direction of the false lumen blood flow and might be moderated by flap motion [30,31]. Additionally, traditional flow visualization methods for patients with aortic dissection are often hindered by the spatial configuration of the true and false lumen and unpredictable branch vessel connectivity. These lumina tend to twist around each other, increasing the complexity of the situation. Therefore, displaying changes in blood flow velocity (T2) and direction (T3) could aid the investigation of these correlations and potentially assist in treatment stratification.

The representation of flow direction (T3), particularly in the evaluation of conditions such as heart valve defects, further necessitates the simultaneous visualization of forward (antegrade) and backward (retrograde) flow [32]. The importance of retrograde flow is further corroborated by Burris et al. [33]. As false lumen pressurization promotes aortic growth [34], the display of false lumen ejection fraction (FLEF), the ratio of retrograde to antegrade flow at the entry tear, gains special relevance.

The configuration of branching vessels that drain the false lumen (false lumen drainage pattern), is associated with late adverse events [9]. FLEF and entry tear dominance (ETD), are both thought to correspond to reduced false lumen drainage through distal openings, which could lead to an increase in false lumen pressure. Currently, there is no straightforward method for assessing the drainage pattern (T4) in aortic dissection. Color-coding flow pathlines based on

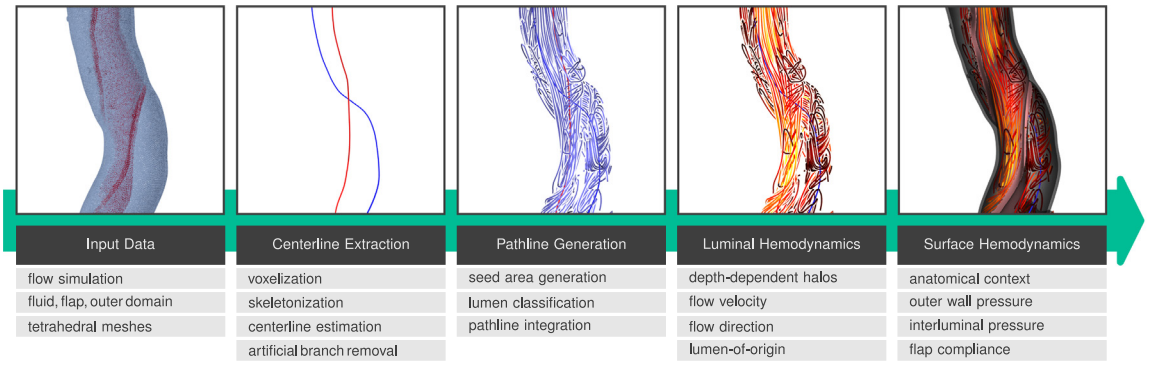

Fig. 1. Workflow for visualizing hemodynamics of aortic dissections. Starting with simulation data as input on the left side, we extract the centerline of the aortic true and false lumen. Proceeding to the right, pathlines are seeded at relevant locations, such as the primary intimal tear, fenestrations, or a reentry tear. Pathlines represent luminal hemodynamics with different color-coding and halos to reduce visual clutter. The flap and outer wall surfaces either serve as context, represent pressure, or convey derived, dissection-specific measures. (Left image created using Paraview [38]).

their lumen would allow experts to examine the originating lumen of a branch's blood supply.

***Use case 2**: Visualization of dissection flap deformation, stiffness, and interluminal pressure difference.* The dissection flap's movement, correlating with the hemodynamics in both lumina, plays a role in the true and false lumen's volume and pressure fluctuations. The flap's stiffness influences this movement, resulting in geometric adaptations to the flow channels owing to varying interluminal pressure gradients. The degree of the flap's motion, revealing its flexibility, changes as the disease progresses. This motion can be irregular, with the flap fluctuating multiple times in a single cardiac cycle and exhibiting inconsistent movement along its length. The cause of such unpredictable flap movements, even in the same cross-section, is yet to be determined. Visualizing the flap's motion and deformation (T5) is critical as it provides insights into these intricate disease dynamics. It elucidates the interplay between various disease factors and could potentially lead to the development of more effective therapeutic strategies or preventative approaches.

Understanding the causes of false lumen pressurization poses a challenge due to the limited availability of interluminal pressure data. Direct measures of pressure differences between true and false lumen can be obtained from CFD simulations in patient-specific geometries [15,17,35]. Indirect measures to estimate pressure, such as FLEF derived from 4D flow MRI measurements [34] or morphological measurements like ETD seen on computed tomography angiography (CTA) scans [36,37], were investigated.

The visualization of interluminal pressure differences (T6) in combination with flap motion could facilitate a better understanding of the driving forces in flap motion and false lumen pressurization, as studied by Marlevi et al. [34]. Additionally, the flap motion is modulated by mechanical properties of the dissection flap, i.e. flap compliance (T7) which can provide insights into the observed stiffness of the dissected tissue.

From a simulation expert's perspective, there is a clear need for such visualization, as there is currently no tool for visualizing these measurements. This technological gap is significant, especially when researching phenomena such as *pressure pulse wave reflection*, which are suspected, but cannot be verified due to the lack of suitable visualization instruments. Clinicians can substantially benefit from advanced visualization of the complex aortic hemodynamics, the interplay between these hemodynamics and flap and wall properties, and the visualization of physiological and pathophysiological phenomena.

***Use case 3**: Effect of dissection-specific blood flow on the false lumen outer wall.* Additional factors could contribute to false lumen pressurization. Patient-specific CFD simulations suggest that the mobility of the dissection flap may alleviate false lumen pressurization [34]. Surgical management may involve creating a fenestration in the flap's distal part, which could decompress the hypertensive false lumen [39]. Visualizing the blood flow through such an artificial luminal communication (T8) would be important to validate the intervention's success.

When blood flows into another lumen via the entry tear or fenestrations, it accelerates, forming a flow jet. Hence, an investigation that only focuses on the flow through a fenestration might not be sufficient. Specifically, complexities arise when such a flow jet strikes the opposing aortic vessel wall, deflecting at what is termed an impingement zone. Visualizing the intricate interrelation between morphological and hemodynamic effects on the false lumen's outer wall and highlighting these zones (T9) is crucial. For radiologists and surgeons, it is pertinent to ascertain if communications are influencing the inflow or outflow. Understanding if any communication significantly impacts hemodynamics is important; closing a hemodynamically significant communication could introduce adverse effects like false lumen growth.

Requirements. After defining the tasks for each use case, we determine their common requirements. Subsequently, we describe the visualization techniques we developed to satisfy all requirements and, ultimately, support all three use cases.

4. Aortic dissection hemodynamics visualization design

The complex anatomy of a dissection and the resulting flow characteristics require special attention and tailored visualization techniques to understand and predict the progression of this disease. In this work, we bridge the gap between individual visualizations for anatomy and hemodynamics of the dissected aorta. As the delamination of the intima wall layer causes the formation of the flap, multiple surfaces need to be displayed to convey the dissected anatomy. Carefully selecting suitable rendering styles for anatomy and hemodynamics is essential to prevent visual overload, especially in their combination. Even more challenging is conveying the hemodynamics of the multiple flow channels. Understanding the complex interplay of the flap with the flow channels of the dissected aorta requires more advanced, derived, and dissection-specific measures.

To summarize the proposed tasks and requirements in a single visualization that conveys both anatomy and luminal as well as surface hemodynamics, a sequence of steps is required (see Fig. 1). It starts with CFD simulations [15] of the entire cardiac cycle at a specified frequency. To define user-specified seed planes for pathline generation, the centerlines of the aorta and both lumina are extracted. Finally, a rendering style is chosen to present the anatomy with the hemodynamics. In the subsequent subsections, we explain our workflow in detail.

4.1. Input data

The surface geometries for the CFD simulations were extracted from CTA data, and two-way FSI simulations were carried out with 4000 time steps in a single cardiac cycle, as described by Bäumler et al. [15]. They compared their simulations results to in-vivo 4D Flow MRI data from the same patient, and found good agreement in terms of vessel wall and flap deformation as well as flow inside both lumina. To provide detailed visualization of the simulation over the entire cardiac cycle at interactive frame-rates, we limit the temporal resolution rather than reducing the spatial resolution. We use 40 evenly-spaced time steps at an interval of 0.8 seconds for a cardiac cycle, leading to a frequency of 50 time steps per second.

These simulations comprise two unstructured tetrahedral meshes, one for the fluid domain (blood) and one for the vessel tissue. The tetrahedral elements of the tissue mesh are further divided into flap domain (dissection flap) and outer domain (outer vessel wall). These domains are used during simulation to distinguish between blood (fluid) and vessel material (deformable solid), and to assign different material properties to the flap and outer domain. Each mesh is associated with hemodynamic and mechanical measurements. These include velocity, pressure, displacement, and derived quantities such as WSS.

4.2. Centerline extraction

The visualization of pathlines requires the definition of seed points, optimally in a cross-section perpendicular to the centerline of a vessel. To accomplish this, we first convert the tetrahedral mesh of the fluid domain into a volumetric representation using voxelization. Subsequently, the skeleton of the fluid domain is extracted [40]. This results in the vessel tree of the true and false lumen in voxel space. We then convert this tree into a directed graph representation [41]. Centerlines of aortic branches and possible erroneous connections between true and false lumen, introduced by skeletonization, are manually removed. This leads to two distinct centerlines, one for the true and false lumen.

4.3. Pathline generation

We compute pathlines to visualize the constantly changing flow fields associated with the hemodynamics of aortic dissection. Selecting a proper seed point is important to reduce cluttering and undersampling artifacts [25]. When integrating pathlines, the velocity vector at a given 3D position needs to be calculated in each integration step. To produce accurate results, we use linear interpolation for, both, space and time. Consequently, the tetrahedral cell containing the currently integrated position has to be located and accessed several times in each integration step. This is a time-consuming operation that can be accelerated as described in the following paragraph.

4.3.1. Grid acceleration structure

Finding the tetrahedral mesh cell corresponding to a particular 3D position usually requires sequentially iterating through the cells of that mesh. To facilitate search in constant time and, consequently, improve rendering performance, an acceleration structure is employed. There are multiple well-known approaches to partition space and accelerate the search process, such as octrees or binary space partition trees [42]. We employ a data structure that partitions space into a grid of cubes with uniform edge length, called grid elements. The space is constituted by the axis-aligned bounding box of the entire tetrahedral mesh. All mesh cells of the outer, flap, and fluid domains are assigned to their corresponding grid element.

The simulation data provides only a single fluid domain that does not distinguish between true and false lumen. However, to obtain this information, we use the grid structure to assign the corresponding flow channel to each cell of the fluid domain. Initially, all grid elements e are unassigned, i.e., labeled as $\mathcal{L}(e) = 0.5$. Cross-sections perpendicular to the true and false lumen centerlines are then computed at regular intervals. Grid elements containing either the true or false lumen portions of these sections are then labeled accordingly, i.e., $\mathcal{L}(e) = 0.0$ and $\mathcal{L}(e) = 1.0$, respectively.

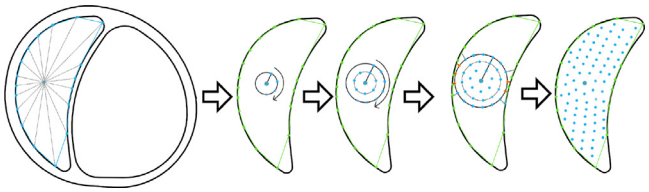

Fig. 2. Illustration of seed area generation and seed point distribution. The lumen's boundary is determined using ray casting from the centerline point outwards. The points are then placed on concentric circles in a constant arc-length interval. Points too close to or beyond the boundary are discarded.

4.3.2. Seed area generation

To choose appropriate seed points, we first define a cross-sectional seed plane along the vessel centerline in an area of interest, e.g., the primary intimal tear, fenestrations, or at the maximal extent of the false lumen. Secondly, we distribute seed points in this plane. Pathlines seeded in the center of the lumen may distribute differently than those seeded at the vessel wall. To avoid overseeing relevant flow patterns, pathlines are distributed evenly across the entire cross-section of the lumen. This is accomplished by casting rays from the centerline point outwards to identify the lumen's boundary (see Fig. 2). Seed points are then evenly placed on circles centered at the centerline point. By successively increasing the radius of the next placement circle while keeping the arc-length distance between points and performing a polygon inside–outside test of every seed point, the entire lumen is filled. Points too close to the vessel wall are rejected. Both, the spacing between points and the minimum distance from the vessel wall are set by the user. We use a spacing of 1.0 mm and a minimum distance of 0.5 mm for all cases presented in this work.

4.3.3. Pathline integration

Starting at the seed point location, the trajectory of a pathline is then computed forward along the vector field. The interpolation of a local velocity vector at a (seed) point utilizes the grid acceleration structure. The position of the next vertex along the pathline is determined using 4th-order Runge–Kutta integration. A pathline is extended until a predetermined maximum number of steps is reached.

Although the velocity vector of fluid–solid interface in FSI simulations is required to conform to the wall motion, the solid domain moves at an identical velocity, resulting in a 'relative' wall velocity of zero. This motion of the solid domain causes pathlines to leave their confining lumen, enter the flap, and possibly continue into the other lumen (see Fig. 3(a)). This phenomenon can also be caused by overly large step sizes during integration and can occur in rigid wall simulations.

To prevent pathlines from crossing the dissection flap or the integration domain, we introduce *early integration termination* of pathlines. Instead of integrating a fixed number of steps, the pathline is stopped when it approaches the vessel wall or the dissection flap too closely (see Fig. 3(b)). This prevents spurious interluminal communications, while still modeling flow through the entry tear, fenestrations, and reentry tears.

4.4. Visualization of luminal hemodynamics

We use pathlines to visualize the hemodynamics provided by the FSI simulation (R01). They can be visualized using different techniques, as surveyed by Brambilla et al. [43], e.g., using lines, ribbons, tubes,

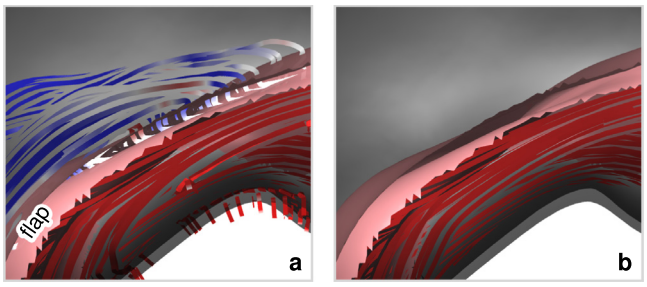

Fig. 3. Artificial communications between true and false lumen caused by incorrectly integrated pathlines. The pathlines shown in (a) originate in the true lumen (red) at the upper right side, spuriously integrate through the flap, and even continue in the false lumen (blue). Our solution confines the pathlines to the true lumen (red), as presented in (b).

or arrows. In this work, pathlines are formed by view-aligned triangle-strips. Flow direction and velocity are conveyed by animated pathlines, i.e., displaying the portion of the path line that corresponds to the current time step of the cardiac cycle (R02).

4.4.1. Depth-dependent halos

While lines and ribbons depict twisted flow well, they tend to cause visual clutter in dense hemodynamic data. To mitigate this problem, we use depth-dependent halos [44]. These halos form a border on both sides of the pathline that only obstructs pathlines further away from the viewer, but not the dissection flap and vessel wall surfaces. This allows the viewer to gauge the depth and distance of intersecting or adjacent pathlines, as shown in Fig. 4.

4.4.2. Flow velocity encoding

The velocity of the blood flow is an important hemodynamics measure to understand complex flow phenomena, such as flow jets. For this reason, we map the magnitude of the flow velocity vector to a heated-body color scale, ranging from black (minimum) to bright yellow (maximum). An example is shown in Fig. 4(a) and this fulfills requirement (R05).

4.4.3. Flow direction encoding

It is particularly important and relevant to observe the development of the already weakened false lumen. To visualize flow direction, we determine the difference between a pathline's direction and the designated luminal flow. For a given position $\mathbf{p}$ on a pathline with velocity vector $\mathbf{v}$ we calculate the corresponding luminal flow direction as the tangent vector $\mathbf{t}$ at the centerline point closest to $\mathbf{p}$. The angle $\gamma = \angle(\mathbf{v}, \mathbf{t})$ then allows us to distinguish between antegrade ($\gamma \leq 90°$) and retrograde ($\gamma > 90°$) flow. To represent a continuous change of direction, we modulate the colors of antegrade and retrograde path lines depending on γ, therefore fulfilling (R06). When using a monochrome color scale from white to red, as shown in Fig. 4(b), the predominant, normal, antegrade flow is shown in white, while the retrograde flow is highlighted.

4.4.4. Lumen-of-origin encoding

To show the originating lumen of branching vessels, we identify the originating lumen of pathlines (R07) based on the lumen classification assigned to each grid element (recall Section 4.3.1). Each pathline starts at a seed point whose lumen label is associated with its enclosing lumen. During integration, the lumen label $\mathcal{L}_t(s)$ of pathline s at time t adapts to the visited grid element $\mathcal{L}_t(e)$ as follows:

$$\mathcal{L}_t(s) = (1-\delta)\mathcal{L}_{t-1}(s) + \delta\mathcal{L}_t(e), \tag{1}$$

with $\delta = 0.05$ controlling the rate of adaptation. This allows pathlines to slowly change their flow channel association when transitioning between channels. Fig. 4(c) shows how this information is displayed using

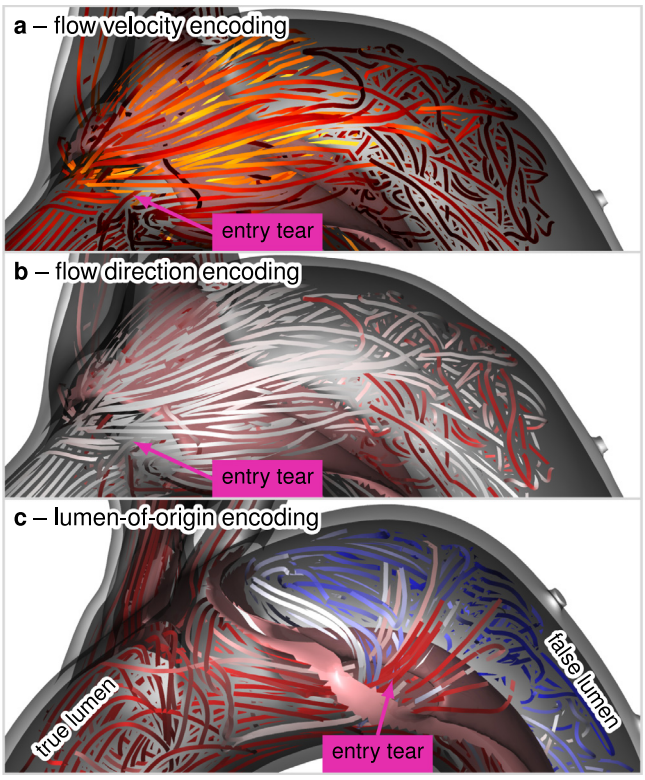

Fig. 4. Pathlines seeded close to an entry tear and color-coded according to various hemodynamic measures. (a) shows flow velocity encoding using a heated-body scale, from black (slow flow) to yellow (fast flow). (b) uses flow direction encoding with a monochrome scale, ranging from white (antegrade flow) to red (retrograde flow). Pathlines with lumen-of-origin encoding are presented in (c) with a diverging color scale from red (true lumen) over white (transitioning) to blue (false lumen).

a diverging color scale, from red (true lumen) over white (transition) to blue (false lumen). The continuous color scale reflects a pathline's gradual change in lumen association and reveals the immediate interaction of the flow at a fenestration, while the contrast between the individual pathlines is reduced when the flow unifies downstream.

4.5. Visualization of anatomy and surface hemodynamics

To fulfill R03 and R04, we display the dissection anatomy with surface meshes. The purpose of this is twofold. When analyzing luminal hemodynamics, the anatomy plays a secondary, contextual role. However, when studying the interaction between flow and flap motion, anatomy plays a primary, focused role.

The visualization of vessel wall motion and, in particular, flap motion facilitates the understanding of the complex luminal hemodynamics of the dissected aorta. For this reason, we represent the tissue motion with surface animation, i.e., by cycling through their deformed meshes of a single cardiac cycle (R08). Surface animation and pathline animation are synchronized to provide an integrated view of blood flow along with vessel motion.

4.5.1. Anatomical context

The visualization of the aortic wall and the dissection flap complements the luminal hemodynamics displayed with pathlines. To create an effective context visualization, we employ shading techniques suggested by Ostendorf et al. [14]. Their study favored Cook-Torrance [45] (specular) combined with Oren-Nayar [46] (diffuse) shading. Fig. 4 shows these styles applied to the dissection flap, the outer vessel wall surfaces, and the pathlines.

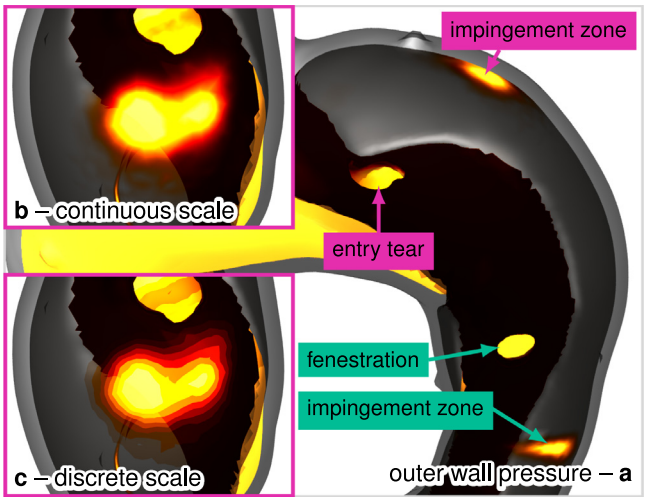

Fig. 5. Pressure color-coded on the aortic outer wall using opacity modulation and a heated-body color scale, from black or dark red (low pressure, transparent) to yellow (high pressure, opaque). (a) shows the descending thoracic aorta with a proximal entry tear and a distal fenestration. A close-up of the impingement zone associated with the entry tear is presented in (b) using a continuous color scale and in (c) with a discrete color scale.

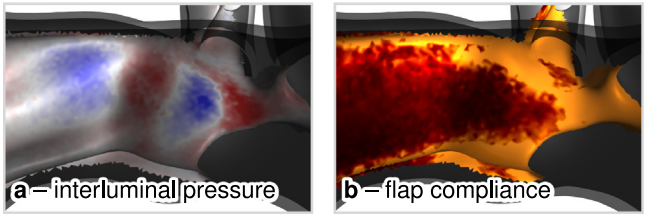

Fig. 6. Flap color-coded with derived, dissection-specific flow measurements. (a) shows the interluminal pressure difference with a diverging color scale, from blue (lower pressure) over white (equal pressure) to red (higher pressure). (b) presents the flap compliance with a heated-body color scale, from black (high compliance) to yellow (low compliance).

4.5.2. Outer wall pressure

Wall pressure is displayed with a heated-body color scale, from black (low) to yellow (high), as shown in Fig. 5. To further emphasize pathological regions with elevated readings while avoiding obstructing flow elsewhere, we perform opacity modulation, i.e., higher values become opaque while lower values become transparent (see Fig. 5(b)). Analogously to importance-driven rendering [47] and semantic visualization mapping [48], this highlights important regions while minimizing obstruction of pathlines in less important regions, thereby satisfying requirements R11 and R12.

Since distinct values are difficult to visually gauge on a continuous scale, we provide a discretized alternative, see Fig. 5(b) vs. Fig. 5(c). The user can interactively control the number of discretization steps and the value range that is mapped to the color scale (similar to the windowing function).

4.5.3. Interluminal pressure difference

Studying the effects of luminal pressure on flap motion (R09) demands a novel, dissection-specific flow measure, namely *interluminal pressure difference* (see Fig. 6). It is defined as the difference in luminal pressure between two corresponding positions on opposite luminal sides of the flap. These positions are calculated using the normal vectors of the luminal surface meshes. This signed and dynamic measurement is visualized with a diverging color scale, with blue (lower pressure) over white (equal pressure) to red (higher pressure).

4.5.4. Dissection flap compliance

Another important objective is recording both, flap motion and interluminal pressure differences (R10). For that reason, we developed *flap compliance*, a derived and dissection-specific measure. It is defined as the ratio of a flap's vertex maximum displacement and absolute interluminal pressure difference. A compliant flap is characterized by a high flap displacement at a low pressure difference, i.e., the flap responds with strong deformation even at a low pressure difference. Low flap displacement and high interluminal pressure indicate a stiffer portion of the flap that is less compliant to the applied pressure. This unsigned and time-independent measurement is visually represented with a heated-body color scale, whereby a high compliance is depicted in black and low compliance in yellow (see Fig. 6(b)).

5. Implementation

The triangular surface meshes of the vessel wall layers and the dissection flap are extracted from the tetrahedral meshes of the CFD simulation (vtu file format) using VTK 9.3.0 [49]. These meshes are then rendered with pathlines using the ray tracing extensions of Vulkan 1.3.224 [50]. Ray tracing has the advantage that shadows, reflections, and transparency are integrated without much effort. These illumination effects facilitate understanding of the aortic anatomy and flow pathlines. Jagged edges at high-contrast lines in image-space, which mainly appear on pathlines, are smoothed with multisample anti-aliasing (MSAA).

Ray tracing is accompanied by some performance disadvantages compared to rasterization especially, when employing anti-aliasing, illumination effects, and transparent surfaces. To mitigate this problem and increase rendering performance, we employ the following two strategies. Firstly, the number of rays cast is reduced by only using a single point light source, approximating surface roughness using Oren-Nayar shading, and limiting the number of reflections. Secondly, the number of MSAA samples is reduced to one when meshes are animated or the camera is moved. This improves frame rates during interaction, while still providing high-quality renderings when stationary.

All visualizations of this paper were created on a desktop computer running Windows 10 Pro with an AMD Ryzen 5 3600 6-Core CPU at 3.59 GHz, 32 GB RAM, and an Nvidia GeForce RTX 2070 GPU. Displaying 55 pathlines with 400 segments each (30000 segments in total), an average of about 30 frames per second (FPS) were achieved. When the camera is stationary and no animation is shown, MSAA is increased, leading to an average of 6 FPS, which is sufficient as the rendered image does not change.

6. Results and discussion

The visualizations for the three use cases described in Section 3 are demonstrated on CFD simulations of three different patients, i.e., one patient per use case. In all cases, the flap is rendered opaque with Cook-Torrance and Oren-Nayar shading and the vessel wall layers are rendered semi-transparently with a Fresnel effect. This visualization allows users to assess the morphology of a dissection. The configuration of the dissection flap, including its extent and curvature are clearly visible through the surface shading. At the same time, the size and shape of the outer aortic wall as well as the location of branching vessels is visible. For each case, we present the entire dataset and then specific regions in detail. We also discuss how the tasks are addressed using our proposed visualizations.

Use case 1 deals with the visualization of true and false lumen blood flow in aortic dissection. Fig. 7(a) presents a type B aortic dissection from the descending thoracic aorta to the left iliac artery, where the exit tear is located. Two specific regions, represented by the colored rectangles, are subsequently explained in more detail.

The first region encompasses the entry tear of the dissection located in the proximal portion of the descending thoracic aorta (magenta

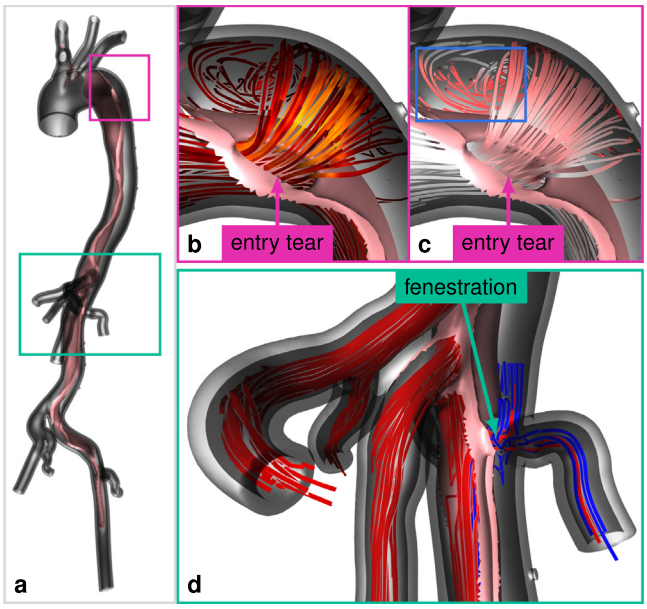

Fig. 7. Use case 1. (a) presents the entire dataset. (b) and (c) depict the proximal portion of the descending thoracic aorta with blood flowing through the entry tear from true lumen into false lumen. (b) displays pathlines with velocity encoding, from slow (black) to fast (yellow) flow. (c) shows flow direction, highlighting retrograde flow in red. (d) shows the renal arteries with lumen-of-origin encoding. The left renal artery is mostly supplied by the false lumen (blue) but also partially by the true lumen (red).

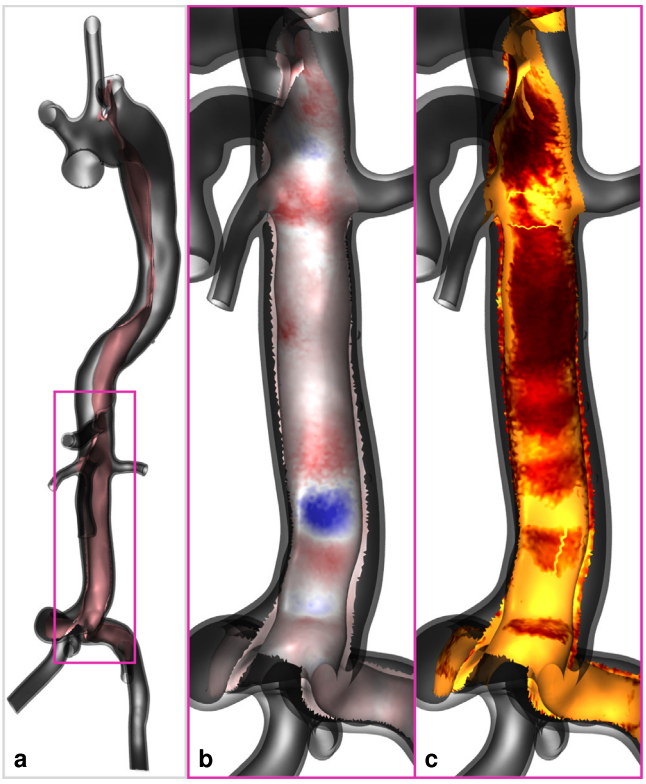

Fig. 8. Use case 2. (a) presents the entire dataset. (b) and (c) show a close-up of the abdominal aorta. In (b) the flap displays the interluminal pressure difference, from blue (lower pressure) to red (higher pressure). The flap compliance is shown in (c), from black (high compliance, mobile) to yellow (low compliance, stiff).

rectangle). Animated pathlines (T1) present the flow through the entry tear and are visualized in Fig. 7(b) with velocity encoding (T2). The pathlines shown in Fig. 7(c) present the flow direction, with regions of retrograde flow being highlighted in red (T3). This particular image displays retrograde flow proximal to the entry tear (see blue rectangle). Visual proof of this backward component of flow in the false lumen suggests a risk of proximal extension of the type B dissection into a potential type A aortic dissection. This progression requires entirely different patient management strategies. While it is currently challenging to predict proximal extension of the dissection, visualizing this information could lead to more informed clinical decisions.

The second area of particular interest pertains to the dissection's drainage pattern (T4). The lumen-of-origin color mapping demonstrates this in Fig. 7(d). All branches of the aorta connect to the true lumen, except the left renal artery. As a consequence of the aortic intima's delamination induced by the dissection, this branch exhibits a fenestration. This allows a portion of the blood from the true lumen to pass through and also sustain this artery, indicated by the red pathline. Malperfusion of organs, such as the kidney, is one of the severe complications associated with aortic dissection. In clinical practice, treatment decisions are often based on an imprecise assessment, as traditional CT imaging does not fully display the perfusion dynamics of the kidney. By providing a more comprehensive visualization of blood flow, clinicians can better estimate the contributions from the true and false lumina to the perfusion of the kidney. In the case of Fig. 7(d), the pathlines reveal that a substantial portion of the renal artery perfusion comes from the false lumen. Clinicians might opt for a more strict monitoring or early surgical intervention to prevent kidney damage.

Fig. 8 demonstrates **use case 2**, which is concerned with the visualization of dissection flap deformation, stiffness, and interluminal pressure difference. This case presents a type B aortic dissection that starts in the aortic arch and extends distally into both iliac arteries, with each having an exit tear, see Bäumler et al. [15].

In this case, we focus on the dissection flap in the abdominal aorta (magenta rectangle) and, in particular, on the flap deformation (T5). To accomplish this, we animate the flap's surface throughout the cardiac cycle. Flap motion is mainly driven by local pressure differences between true and false lumen. This is conveyed by our introduced measure *interluminal pressure difference* (T6), as displayed in Fig. 8(b).

When combining both, flap motion and interluminal pressure difference, the flap's local stiffness becomes apparent. This newly proposed measure, called *flap compliance* (T7), has not yet been studied in aortic dissection research but may provide insight into local flap dynamics. As shown in Fig. 8(c), highlighted regions deform less drastically in response to high pressure differences (yellow) compared to more mobile regions (dark red).

Use case 3 highlights the presence of a flow jet through a fenestration in a type B aortic dissection that starts at the beginning of the descending thoracic aorta and reaches distally just before the celiac trunk.

The analyst starts by examining the anatomy of the vessel to locate regions-of-interest. One of these interesting regions are fenestrations, because they affect false lumen dilatation. To assess the blood flow through a fenestration, pathlines are generated in its proximity and, subsequently, animated during inspection (T8). Without color cues, it is difficult to determine from which lumen a pathline originates and where it leads (see Fig. 9(b)). Our lumen-of-origin encoding on the pathlines shows which lumen supplies the blood through the fenestration (red, true) and which receives it (blue, false). As the pathlines transit through the fenestration, they gradually change their color from red to blue over white, as displayed in Fig. 9(c).

This visual encoding can also be used to inspect the effect of flow jets on the opposite vessel wall, so-called impingement zones (T9). Since pathlines are contextual information in this situation, they are displayed without colors. The focused impingement zone is represented with a discrete heated-body color scale that conveys the local pressure.

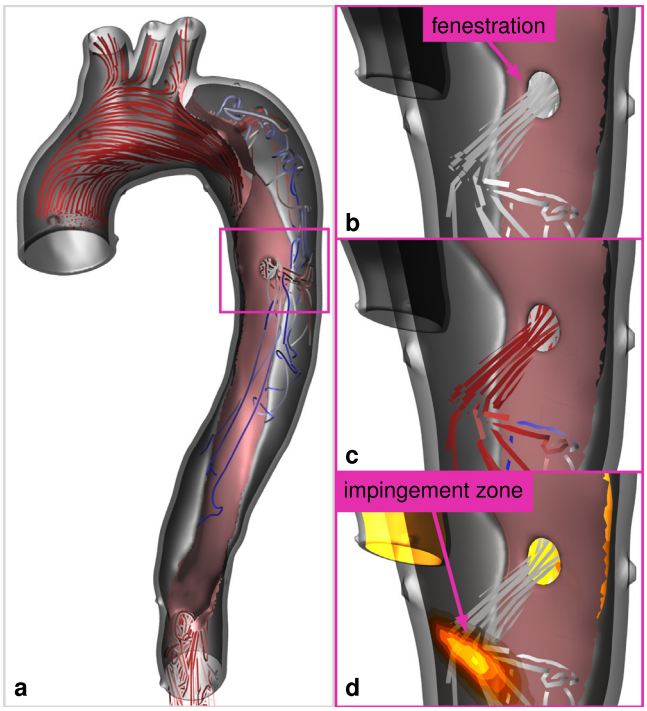

Fig. 9. Use case 3. (a) represents the entire dataset with a synthetic fenestration in the descending thoracic aorta. The pathlines shown originate in the true lumen (red) and transit (white) through the entry tear and fenestration into the false lumen (blue). Since the color transition starts at the luminal communication, the delayed transition to blue allows users to clearly identify the origin of the lumen. (b) and (c) depict a close-up of blood flow through the fenestration, without color-coding and with lumen-of-origin encoding, respectively. The effect of the flow jet on the outer vessel wall, the impingement zone, is displayed in (d) with a discrete color scale and opacity modulation. A heated-body color scale is used, which maps low pressure to black and high pressure to yellow. The opacity is proportional to pressure.

In addition, opacity modulation makes areas of low pressure on the wall surface transparent (see Fig. 9(d)).

Localized impingement zones with high-pressure flow jets could lead to more aggressive tissue remodeling, potentially increasing the risk of aneurysm formation or rupture. This information can prompt clinicians to monitor these areas more closely or consider preemptive interventions to mitigate the risks. Moreover, understanding the characteristics of impingement zones can motivate future research into the mechanical and biological responses of aortic tissue to different flow patterns. Investigating how these zones influence tissue remodeling could lead to new therapeutic strategies aimed at reinforcing vulnerable areas of aortic dissection progression and develop more targeted and effective treatment approaches.

Limitations. Our current workflow (see Fig. 1) involves two predominantly manual and time-consuming components: the generation of a vessel tree and pathline generation. We provide a discussion of these components below, including possible enhancements.

Building a dissection-specific vessel tree is a complex and demanding task [13]. Initially, we manually edited the vessel tree to adhere with our requirements. Nevertheless, this step could be bolstered with the assistance of automatic segmentation methods [51–53], leading not only to a reduction in required time but also an improved reproducibility.

Pathline generation, particularly the determination of their seeding location, is the second component. Identifying suitable seeding locations to examine flow phenomena, like impingement zones after fenestrations, is vital but notably time-consuming. Furthermore, the density and distribution of pathlines in the seeding area influence the overall depiction. For instance, densely arranged pathlines might obstruct certain phenomena. Implementing smart interactive filtering strategies could enhance this component [54].

7. Evaluation

To formulate an appropriate set of questions (see Table 2), we conducted a pilot study with a small group of radiologists experienced in aortic dissections. The results of this preliminary study were not included in the final analysis.

The primary evaluation was conducted in two separate online sessions during weekly endovascular and vascular surgery conferences, with the goal to present our visualization to a large audience. Participants were cardiothoracic and vascular surgeons possessing substantial experience in management of patients suffering from aortic dissection. A total of 16 questions were asked, distributed across the three use cases (recall Section 3) with **UC1: Q1-Q9**, **UC2: Q10-Q12**, and **UC3: Q13-Q15**. Each question was associated with either a 10 s video or a still image showing the respective visualization. Additionally, a series of answers were shown on a Likert scale.[1] Participants were then asked to post their answers (Likert score) into the open chat of the virtual conference. The entire session was recorded for later extraction of results. We had contributions from 20 unique participants (including one of the co-authors) spread across the two sessions, with 15 contributing in the first session and 5 in the second. The combined results from both sessions are presented in Table 2 and subsequent descriptive statistics are reported as median and interquartile range (IQR).

The combined visualization of anatomy and flow (**Q1**: 4 (3-4)) was mainly rated as helpful. Color-coding improved both, the assessment of flow direction (**Q2**: 3 (3-4) vs **Q3**: 5 (4-5)), and velocity (**Q4**: 3 (2-3) vs **Q5**: 4 (4-5)). Using lumen-of-origin encoding on pathlines that transit through a fenestration showed no difference to the uncolored ones (**Q6**: 100% vs **Q7**: 100% correct answers), although two participants explicitly mentioned clarity was improved. For assessing the drainage pattern, lumen-of-origin encoding was decisive (**Q8**: 21.4% vs **Q9**: 64.3% correct answers), especially with complex hemodynamics such as fenestrations near branching vessels. Two participants rated the vessel supply as unclear, while two participants indicated that they could even approximate the amount of blood supply to a branch based on the colors. Participants consistently rated surface animation (**Q10**: 4 (4-4)), interluminal pressure difference (**Q11**: 4 (4-4)), and flap compliance (**Q12**: 4 (3-5)) as helpful. The evaluation showed that the location and extent of impingement zones caused by flow jets cannot be derived from the anatomy alone (**Q13**: 2 (2-3)). Adding pathlines considerably increased the participants' confidence (**Q14**: 4 (4-5)). This was further corroborated by color-coding the pressure on the vessel wall (**Q15**: 5 (5-5)).

Throughout the development of our hemodynamics visualizations, we noticed the occurrence of interluminal pressure gradients moving along the dissection flap. We speculated that this could represent a pressure wave (see Fig. 9(b)) that moves distally during systole and relocates proximally shortly after. This phenomenon was hypothesized to exist but had never been visualized before. The intent of **Q16** was to validate this observation. All participants confirmed the movement as oscillatory in nature. One participant suggested that it might be the reflection of a pulse wave in the distal parts of the vessel.

8. Conclusion and future work

Several factors are thought to contribute to false lumen degeneration, unfavorable tissue response, and thrombus formation [8,31]. To

[1] Link to the complete evaluation material

Table 2
Evaluation of our visualizations. We start with a brief description of the presented visualization, followed by the question itself and the participants' answers. The answer scales and choices are shown at the bottom. Results are reported as median and interquartile range (IQR). The questions are grouped by UC1: Q1-Q9, UC2: Q10-Q12, and UC3: Q13-Q15.

No.	Scale	Median	IQR	Answers
Q1	1	4	3 - 4	3 3 3 3 4 4 4 4 4 4 4 4 4 5
Description: Pan over the dataset in Fig. 8. Pathlines uncolored. Surfaces and pathlines animated. *Question: Please rate the visualization for the distinction of true and false lumen anatomy and flow.*				
Q2	2	3	3 - 4	2 3 3 3 3 3 3 3 3 4 4 4 4 4 4 4 5
Description: View of the dataset in Fig. 8. Pathlines uncolored. Surfaces and pathlines animated. *Question: How confident are you in identifying retrograde flow?*				
Q3	2	5	4 - 5	3 4 4 4 4 5 5 5 5 5 5 5 5 5 5 5
Description: Same as Q2. Pathlines with flow direction encoding. *Question: How confident are you in identifying retrograde flow?*				
Q4	2	3	2 - 3	1 2 2 2 2 2 2 3 3 3 3 3 4 4 5
Description: Same as Q2. *Question: How confident are you in identifying regions of high velocity flow?*				
Q5	2	4	4 - 5	2 4 4 4 4 4 4 4 4 5 5 5 5 5 5 5 5
Description: Same as Q2. Pathlines with velocity encoding. *Question: How confident are you in identifying region of high velocity flow?*				
Q6	3	A	A-A	A, A, A, A, A, A, A, A, A, A, A, A, A, A, A
Description: View of the dataset in Fig. 9. Pathlines uncolored. Surfaces and pathlines animated. *Question: Which lumen does the flow jet originate from?*				
Q7	3	A	A-A	A, A, A, A, A, A, A, A, A, A, A, A, A, A, A
Description: Same as Q6. Pathlines with lumen-of-origin. *Question: Which lumen does the flow jet originate from?*				
Q8	4	B	B-B	A, B, B, B, B, B, B, B, B, B, B, C, C, C
Description: View of the dataset in Fig. 7. Pathlines uncolored. Surfaces and pathlines animated. *Question: Which lumen supplies the vessel marked with an arrow?*				
Q9	4	C	B-C	A, B, B, B, B, C, C, C, C, C, C, C, C, C
Description: Same as Q8. Pathlines with lumen-of-origin encoding. *Question: Which lumen supplies the vessel marked with an arrow?*				
Q10	1	4	4 - 4	3 4 4 4 4 4 4 4 4 4 4 4 4 5 5
Description: View of the dataset in Fig. 8. No pathlines shown. Surfaces animated. *Question: Please rate the value of surface animation for the assessment of flap deformation.*				
Q11	1	4	4 - 4	3 4 4 4 4 4 4 4 4 4 4 4 4 5
Description: Same as Q10. Flap with interluminal pressure difference encoding. *Question: Please rate the value of surface animation for the assessment of flap deformation.*				
Q12	1	4	3 - 5	3 3 3 3 3 4 4 4 4 5 5 5 5
Description: Same as Q10. Flap with compliance encoding. *Question: Please rate the value of surface animation for the assessment of flap deformation.*				
Q13	2	2	2 - 3	1 1 2 2 2 3 3 3 3 3
Description: View of the dataset in Fig. 9. No pathlines. Surfaces animated. *Question: How confident are you assessing location and extent of the impingement zone.*				
Q14	2	4	4 - 5	3 3 4 4 4 4 4 5 5 5
Description: Same as Q13. Pathlines uncolored. Surfaces and pathlines animated. *Question: How confident are you assessing location and extent of the impingement zone.*				
Q15	2	5	5 - 5	2 4 4 5 5 5 5 5 5 5 5 5
Description: Same as Q14. Outer vessel wall with pressure encoding. *Question: How confident are you assessing location and extent of the impingement zone.*				
Q16	5	D	D-D	D, D, D, D, D, D, D, D, D, D
Description: View of the dataset in Fig. 8. Flap with interluminal pressure difference encoding. No pathlines. Surfaces animated. *Question: Describe the movement of pressure gradients on the dissection flap.*				

Scales

1	Highly Misleading (1) – Misleading (2) – Neutral (3) – Helpful (4) – Highly Helpful (5)
2	Highly Unconfident (1) – Unconfident (2) – Neutral (3) – Confident (4) – Highly Confident (5)
3	Lumen A (A) – Lumen B (B) A = true lumen (correct), B = false lumen
4	Lumen A (A) – Lumen B (B) – Both Lumina (C) A = true lumen, B = false lumen, C = both lumina (correct)
5	Static (A) – Moving Antegrade (B) – Moving Retrograde (C) – Oscillating (D)

date, their complex interplay is yet to be understood. Furthermore, despite the availability of various data, their interpretation is challenging and benefits greatly from novel visualization techniques that highlight complex relationships between pressure, flow, mechanical forces, and wall movement in a given dissection anatomy.

In this work we contribute to the understanding of aortic dissection hemodynamics, a transdisciplinary research endeavor [55]. To comprehend flow measurements in relation to the shape and volume of true and false lumen, we display the dissection flap and the outer vessel wall as context. Besides color-coding existing hemodynamic

measurements on pathlines and vessel wall surfaces, we introduced two derived measures to study the interplay of both lumina. Both are visually encoded on the flap. The first depicts the interluminal pressure difference and the second relates this measure with the flap's ability to deform in response to those pressure differences. Flap deformation was shown through surface animation. Together with animated pathlines, our visualization simultaneously depicts the dynamics of blood and vessel tissue in the dissected aorta during the cardiac cycle.

To corroborate the clinical value of our contributions, we conducted an evaluation with experts on cardiothoracic and vascular surgery. It was executed in a virtual setting to reach a larger audience, and the overall response was favorable. Above all, new insights were gained that can promote new ideas for downstream surgical decision-making. To draw a more informed conclusion, a more profound study, which could involve participants directly interacting with the application (guided evaluation) and streamlined workflow are required, both of which being subject to future work.

CRediT authorship contribution statement

Aaron Schroeder: Writing – review & editing, Writing – original draft, Visualization, Software, Project administration, Methodology, Data curation, Conceptualization. **Kai Ostendorf:** Writing – review & editing, Writing – original draft, Software, Methodology, Conceptualization. **Kathrin Bäumler:** Writing – review & editing, Writing – original draft, Data curation, Conceptualization. **Domenico Mastrodicasa:** Writing – review & editing, Writing – original draft, Conceptualization. **Veit Sandfort:** Writing – review & editing, Conceptualization. **Dominik Fleischmann:** Writing – review & editing, Writing – original draft, Conceptualization. **Bernhard Preim:** Writing – review & editing, Supervision. **Gabriel Mistelbauer:** Writing – review & editing, Writing – original draft, Supervision, Software, Methodology, Conceptualization.

Data availability

The authors do not have permission to share data.

Acknowledgments

The medical data set shown in Fig. 7 were acquired at Stanford School of Medicine, approved by the institutional review board (IRB#41660). The datasets shown in Fig. 8 and Fig. 9 are available at https://www.vascularmodel.com Open access funding enabled and organized by Projekt DEAL.

Declaration of competing interest

The authors declare that they have no known competing financial interests or personal relationships that could have appeared to influence the work reported in this paper.

Appendix A. Supplementary data

Supplementary material related to this article can be found online at https://doi.org/10.1016/j.cag.2024.104060.

References

[1] Wundram M, Falk V, Eulert-Grehn J-J, Herbst H, Thurau J, Leidel BA, et al. Incidence of acute type A aortic dissection in emergency departments. Sci Rep 2020;10(1):7434. http://dx.doi.org/10.1038/s41598-020-64299-4.

[2] Spinelli D, Benedetto F, Donato R, Piffaretti G, Marrocco-Trischitta M, Patel H, et al. Current evidence in predictors of aortic growth and events in acute type B aortic dissection. J Vasc Surg 2018;68(6):1925–35. http://dx.doi.org/10.1016/j.jvs.2018.05.232.

[3] Mastrodicasa D, Willemink MJ, Turner VL, Hinostroza V, Codari M, Hanneman K, et al. Registry of aortic diseases to model adverse events and progression (ROADMAP) in uncomplicated type B aortic dissection: Study design and rationale. Radiol Cardiothorac Imaging 2022;4(6):1–7. http://dx.doi.org/10.1148/ryct.220039.

[4] Chung JW, Elkins C, Sakai T, Kato N, Vestring T, Semba C, et al. True-lumen collapse in aortic dissection: part I. Evaluation of causative factors in phantoms with pulsatile flow. Radiology 2000;214(1):87–98. http://dx.doi.org/10.1148/radiology.214.1.r00ja3287.

[5] Chung JW, Elkins C, Sakai T, Kato N, Vestring T, Semba CP, et al. True-lumen collapse in aortic dissection: part II. Evaluation of treatment methods in phantoms with pulsatile flow. Radiology 2000;214(1):99–106. http://dx.doi.org/10.1148/radiology.214.1.r00ja3499.

[6] Berguer R, Parodi J, Schlicht M, Khanafer K. Experimental and clinical evidence supporting septectomy in the primary treatment of acute type B thoracic aortic dissection. Ann Vasc Surg 2015;29(2):167–73. http://dx.doi.org/10.1016/j.avsg.2014.10.001.

[7] Tsai TT, Schlicht MS, Khanafer K, Bull JL, Valassis DT, Williams DM, et al. Tear size and location impacts false lumen pressure in an ex vivo model of chronic type B aortic dissection. J Vasc Surg 2008;47(4):844–51. http://dx.doi.org/10.1016/j.jvs.2007.11.059.

[8] Cheng Z, Tan F, Riga C, Bicknell C, Hamady M, Gibbs R, et al. Analysis of flow patterns in a patient-specific aortic dissection model. J Biomech Eng 2010;132(5):051007. http://dx.doi.org/10.1115/1.4000964.

[9] Sailer A, Kuijk S, Nelemans P, Chin A, Kino A, Huininga M, et al. Computed tomography imaging features in acute uncomplicated stanford type-B aortic dissection predict late adverse events. Circ Cardiovasc Imag 2017;10(4):e005709. http://dx.doi.org/10.1161/CIRCIMAGING.116.005709.

[10] Clough RE, Waltham M, Giese D, Taylor PR, Schaeffter T. A new imaging method for assessment of aortic dissection using four-dimensional phase contrast magnetic resonance imaging. J Vasc Surg 2012;55(4):914–23. http://dx.doi.org/10.1016/j.jvs.2011.11.005.

[11] Marsden A. Simulation based planning of surgical interventions in pediatric cardiology. Phys Fluids 2013;25(10):101303. http://dx.doi.org/10.1063/1.4825031.

[12] Taylor C, Steinman D. Image-based modeling of blood flow and vessel wall dynamics: Applications, methods and future directions. Ann Biomed Eng 2010;38(3):1188–203. http://dx.doi.org/10.1007/s10439-010-9901-0.

[13] Mistelbauer G, Rössl C, Bäumler K, Preim B, Fleischmann D. Implicit modeling of patient-specific aortic dissections with elliptic Fourier descriptors. Comput Graph Forum 2021;40(3):423–34. http://dx.doi.org/10.1111/cgf.14318.

[14] Ostendorf K, Mastrodicasa D, Bäumler K, Codari M, Turner V, Willemink MJ, et al. Shading style assessment for vessel wall and lumen visualization. In: Eurographics workshop on visual computing for biology and medicine. The Eurographics Association; 2021, http://dx.doi.org/10.2312/VCBM.20211350.

[15] Bäumler K, Vedula V, Sailer A, Seo J, Chiu P, Mistelbauer G, et al. Fluid–structure interaction simulations of patient-specific aortic dissection. Biomech Model Mechanobiol 2020;19(5):1607–28. http://dx.doi.org/10.1007/s10237-020-01294-8.

[16] Cheng Z, Wood N, Gibbs R, Xu X. Geometric and flow features of type B aortic dissection: Initial findings and comparison of medically treated and stented cases. Ann Biomed Eng 2014;43(1):177–89. http://dx.doi.org/10.1007/s10439-014-1075-8.

[17] Xu H, Xiong J, Han X, Mei Y, Shi Y, Wang D, et al. Computed tomography-based hemodynamic index for aortic dissection. J Thorac Cardiovasc Surg 2021;162(2):e165–76. http://dx.doi.org/10.1016/j.jtcvs.2020.02.034.

[18] Karmonik C, Bismuth J, Shah D, Davies M, Purdy D, Lumsden A. Computational study of haemodynamic effects of entry- and exit-tear coverage in a DeBakey type III aortic dissection: technical report.. Eur J Vasc Endovasc Surg 2011;42 2(2):172–7. http://dx.doi.org/10.1016/j.ejvs.2011.04.008.

[19] Yu S, Liu W, Wong R, Underwood M, Wang D. The potential of computational fluid dynamics simulation on serial monitoring of hemodynamic change in type B aortic dissection. Cardiovasc Intervent Radiol 2016;39(8):1090–8. http://dx.doi.org/10.1007/s00270-016-1352-z.

[20] Dillon-Murphy D, Noorani A, Nordsletten D, Figueroa CA. Multi-modality image-based computational analysis of haemodynamics in aortic dissection. Biomech Model Mechanobiol 2016;15(4):857–76. http://dx.doi.org/10.1007/s10237-015-0729-2.

[21] Oeltze-Jafra S, Meuschke M, Neugebauer M, Saalfeld S, Lawonn K, Janiga G, et al. Generation and visual exploration of medical flow data: Survey, research trends, and future challenges. Comput Graph Forum 2018;38. http://dx.doi.org/10.1111/cgf.13394.

[22] Gasteiger R, Neugebauer M, Kubisch C, Preim B. Adapted surface visualization of cerebral aneurysms with embedded blood flow information. In: Proceedings of the eurographics workshop on visual computing for biology and medicine. 2010, http://dx.doi.org/10.2312/VCBM/VCBM10/025-032.

[23] Lawonn K, Gasteiger R, Preim B. Adaptive surface visualization of vessels with animated blood flow. Comput Graph Forum 2014;33(8):16–27. http://dx.doi.org/10.1111/cgf.12355.

[24] Behrendt B, Berg P, Preim B, Saalfeld S. Combining pseudo chroma depth enhancement and parameter mapping for vascular surface models. In: Proceedings of the eurographics workshop on visual computing for biology and medicine. 2017, p. 159–68. http://dx.doi.org/10.2312/vcbm.20171250.

[25] Behrendt B, Engelke W, Berg P, Beuing O, Hotz I, Preim B, et al. Visual exploration of intracranial aneurysm blood flow adapted to the clinical researcher. In: Eurographics – dirk bartz prize. The Eurographics Association; 2021.

[26] Köhler B, Grothoff M, Gutberlet M, Preim B. Bloodline: A system for the guided analysis of cardiac 4D PC-MRI data. Comput Graph 2019.

[27] Straka M, Cervenansky M, Cruz AL, Köchl A, Šrámek M, Gröller E, et al. The VesselGlyph: Focus & context visualization in CT-angiography. In: Proceedings of IEEE visualization. 2004, p. 385–92. http://dx.doi.org/10.1109/VISUAL.2004.104.

[28] Glaßer S, Lawonn K, Hoffmann T, Skalej M, Preim B. Combined visualization of wall thickness and wall shear stress for the evaluation of aneurysms. IEEE Trans Vis Comput Graphics 2014;20(12):2506–15. http://dx.doi.org/10.1109/tvcg.2014.2346406.

[29] Lawonn K, Glaßer S, Vilanova A, Preim B, Isenberg T. Occlusion-free blood flow animation with wall thickness visualization. IEEE Trans Vis Comput Graphics 2016;22(1):728–37. http://dx.doi.org/10.1109/tvcg.2015.2467961.

[30] Evangelista A, Salas A, Ribera A, Ferreira-González I, Cuéllar H, Pineda V, et al. Long-term outcome of aortic dissection with patent false lumen: predictive role of entry tear size and location. Circulation 2012;125(25):3133–41. http://dx.doi.org/10.1161/CIRCULATIONAHA.111.090266.

[31] Fleischmann D, Afifi RO, Casanegra AI, Elefteriades JA, Gleason TG, Hanneman K, et al. Imaging and surveillance of chronic aortic dissection: A scientific statement from the American heart association. Circ Cardiovasc Imag 2022;15(3). http://dx.doi.org/10.1161/hci.0000000000000075.

[32] Carroll RJ, Falsetti HL. Retrograde coronary artery flow in aortic valve disease. Circulation 1976;54(3):494–9. http://dx.doi.org/10.1161/01.CIR.54.3.494.

[33] Burris NS, Patel HJ, Hope MD. Retrograde flow in the false lumen: Marker of a false lumen under stress? J Thorac Cardiovasc Surg 2019;157(2):488–91. http://dx.doi.org/10.1016/j.jtcvs.2018.06.092.

[34] Marlevi D, Sotelo JA, Grogan-Kaylor R, Ahmed Y, Uribe S, Patel HJ, et al. False lumen pressure estimation in type B aortic dissection using 4D flow cardiovascular magnetic resonance: comparisons with aortic growth. J Cardiovasc Magn Reson 2021;23(1). http://dx.doi.org/10.1186/s12968-021-00741-4.

[35] Ong CW, Wee I, Syn N, Ng S, Leo HL, Richards AM, et al. Computational fluid dynamics modeling of hemodynamic parameters in the human diseased aorta: A systematic review. Ann Vasc Surg 2020;63:336–81. http://dx.doi.org/10.1016/j.avsg.2019.04.032.

[36] Fleischmann D, Burris N. Entry tear dominance at CT angiography predicts long-term clinical outcomes in aortic dissection: Another piece of the puzzle. Radiol Cardiothorac Imaging 2021;3(6). http://dx.doi.org/10.1148/ryct.2021210271.

[37] Cuellar-Calabria H, Burcet G, Roque A, Rodríguez-Palomares J, Teixidó G, Rodríguez R, et al. Differences in the area of proximal and distal entry tears at CT angiography predict long-term clinical outcomes in aortic dissection. Radiol Cardiothorac Imaging 2021;3(6). http://dx.doi.org/10.1148/ryct.2021210029.

[38] Utkarsh A. The paraview guide: A parallel visualization application. Kitware Inc.; 2015.

[39] Hartnell GG, Gates J. Aortic fenestration: A why, when, and how-to guide. RadioGraphics 2005;25(1):175–89. http://dx.doi.org/10.1148/rg.251045078.

[40] Lee T-C, Kashyap RL, Chu C-N. Building skeleton models via 3-D medial surface/axis thinning algorithms. CVGIP, Graph Models Image Process 1994;56(6):462–78. http://dx.doi.org/10.1006/cgip.1994.1042.

[41] Mistelbauer G. Smart interactive vessel visualization in radiology [Ph.D. thesis], Faculty of Computer Science of the Technical University of Vienna; 2013, http://dx.doi.org/10.34726/hss.2013.22462.

[42] Yenpure A, Sane S, Binyahib R, Pugmire D, Garth C, Childs H. State-of-the-art report on optimizing particle advection performance. Comput Graph Forum 2023. http://dx.doi.org/10.1111/cgf.14858.

[43] Brambilla A, Carnecky R, Peikert R, Viola I, Hauser H. Illustrative flow visualization: State of the art, trends and challenges. In: Cani M-P, Ganovelli F, editors. Eurographics 2012 – state of the art reports. 2012, p. 75–94. http://dx.doi.org/10.2312/conf/EG2012/stars/075-094.

[44] Everts MH, Bekker H, Roerdink JBTM, Isenberg T. Depth-dependent halos: Illustrative rendering of dense line data. IEEE Trans Vis Comput Graphics 2009;15(6):1299—-306. http://dx.doi.org/10.1109/TVCG.2009.138.

[45] Cook RL, Torrance KE. A reflectance model for computer graphics. ACM Trans Graph 1982;1(1):7–24. http://dx.doi.org/10.1145/357290.357293.

[46] Oren M, Nayar S. Generalization of Lambert's reflectance model. In: Schweitzer D, editor. Computer graphics and interactive techniques. New York, NY: ACM Press; 1994, p. 239–46. http://dx.doi.org/10.1007/BF01679684.

[47] Viola I, Feixas M, Sbert M, Gröller ME. Importance-driven focus of attention. IEEE Trans Vis Comput Graphics 2006;12(5):933–40. http://dx.doi.org/10.1109/TVCG.2006.152.

[48] Rautek P, Bruckner S, Gröller ME. Semantic layers for illustrative volume rendering. IEEE Trans Vis Comput Graphics 2007;13(6):1336–43. http://dx.doi.org/10.1109/TVCG.2007.70591.

[49] Schroeder W, Martin K, Lorensen B. The visualization toolkit. 4th ed. Kitware Inc.; 2006.

[50] The Khronos® Group Inc J. Vulkan — cross platform 3D graphics. 2022, https://www.vulkan.org/.

[51] Hahn LD, Mistelbauer G, Higashigaito K, Koci M, Willemink MJ, Sailer AM, et al. CT-based true- and false-lumen segmentation in type b aortic dissection using machine learning. Radiol Cardiothorac Imaging 2020;2(3):e190179. http://dx.doi.org/10.1148/ryct.2020190179.

[52] Xiang D, Qi J, Wen Y, Zhao H, Zhang X, Qin J, et al. ADSeg: A flap-attention-based deep learning approach for aortic dissection segmentation. Patterns 2023;4(5):1–14. http://dx.doi.org/10.1016/j.patter.2023.100727.

[53] Zhang J, Liu J, Wei S, Chen D, Xiong J, Gao F. Semi-supervised aortic dissections segmentation: A time-dependent weighted feedback fusion framework. Comput Med Imaging Graph 2023;106:1–9. http://dx.doi.org/10.1016/j.compmedimag.2023.102219.

[54] Behrendt B, Berg P, Beuing O, Preim B, Saalfeld S. Explorative Blood Flow Visualization Using Dynamic Line Filtering Based on Surface Features. Comput Graph Forum 2018;37(3):183–94. http://dx.doi.org/10.1111/cgf.13411.

[55] Mistelbauer G, Bäumler K, Mastrodicasa D, Hahn LD, Pepe A, Sandfort V, et al. Transdisciplinary visualization of aortic dissections. In: Kuhlen TW, Raidou RG, editors. EuroVis 2023 – dirk bartz prize. 2023, p. 1–5. http://dx.doi.org/10.2312/evm.20231085.